

STAMP: Differentiable Task and Motion Planning via Stein Variational Gradient Descent

Yewon Lee¹, Andrew Z. Li¹, Philip Huang², Eric Heiden³, Krishna Murthy Jatavallabhula⁴,
Fabian Damken^{1,5}, Kevin Smith⁴, Derek Nowrouzezahrai⁶, Fabio Ramos^{3,7}, Florian Shkurti¹

Abstract—Planning for sequential robotics tasks often requires integrated symbolic and geometric reasoning. Task and Motion Planning (TAMP) algorithms typically solve these problems by performing a tree search over high-level task sequences while checking for kinematic and dynamic feasibility. This can be inefficient because, typically, candidate task plans resulting from the tree search ignore geometric information. This often leads to motion planning failures that require expensive backtracking steps to find alternative task plans. We propose a novel approach to TAMP called Stein Task and Motion Planning (STAMP) that relaxes the hybrid optimization problem into a continuous domain. This allows us to leverage gradients from differentiable physics simulation to fully optimize discrete and continuous plan parameters for TAMP. In particular, we solve the optimization problem using a gradient-based variational inference algorithm called Stein Variational Gradient Descent. This allows us to find a distribution of solutions within a single optimization run. Furthermore, we use an off-the-shelf differentiable physics simulator that is parallelized on the GPU to run parallelized inference over diverse plan parameters. We demonstrate our method on a variety of problems and show that it can find multiple diverse plans in a single optimization run while also being significantly faster than existing approaches. <https://rvl.cs.toronto.edu/stamp>

I. INTRODUCTION

Task and Motion Planning (TAMP) is central to many sequential decision-making problems in robotics, which often require integrated logical and geometric reasoning to generate a feasible symbolic action and motion plan that achieves a particular goal [1]. In this paper, we present a novel algorithm called Stein Task and Motion Planning (STAMP), which uses Stein variational gradient descent (SVGD) [2], [3], a variational inference method, to efficiently generate a distribution of optimal solutions in a single run. Unlike existing methods, we transform TAMP problems, which operate over both discrete symbolic variables and continuous motion variables, into the continuous domain. This allows us to run gradient-based inference using SVGD and differentiable physics simulation to generate a diversity of plans.

Prior works such as [4], [5], [6], [7], [8] solve TAMP problems by performing a tree search over discrete logical plans and integrating this with motion optimization and feasibility checking. By leveraging gradient information, STAMP forgoes the need to conduct a computationally expensive tree search that might involve backtracking and might be hard to parallelize. Instead, STAMP infers the

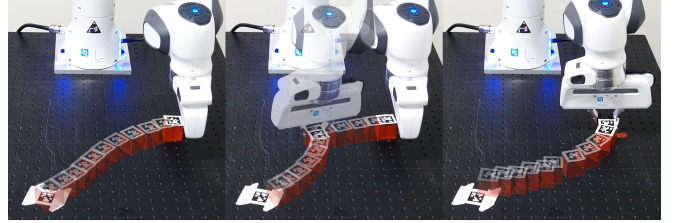


Fig. 1. Demonstrations of the top-3 block-pushing plans found by STAMP on a Franka manipulator. Task plans from left to right: push the East side; push the East side, then the North side; push the North side. STAMP found all three solutions in one run.

relaxed logical action sequences jointly with continuous motion plans, without a tree search.

Further, by solving a Bayesian inference problem over the search space and utilizing GPU parallelization, STAMP conducts a parallelized optimization over multiple logical and geometric plans at once. As a result, it produces large, diverse plan sets that are crucial in downstream tasks with replanning, unknown user preferences, or uncertain environments. While several diverse planning methods have been developed for purely symbolic planning [9], [10], most TAMP algorithms do not explicitly solve for multiple plans and suffer from an exploration-versus-computation time trade-off.

Why would we need multiple solutions if only one will eventually be executed? One reason is that having access to a diverse set of solutions provides added flexibility in selecting a feasible plan based on criteria that were not initially considered. Second, the push for diverse solutions might lead to unexpected, but feasible plans. Third, when TAMP is used as a generating process for training data for imitation learning [11], a diverse set of solutions is preferable to learn policies that induce multi-modal trajectory distributions.

The main contributions of our work are (a) introducing a relaxation of the discrete symbolic actions and thus reformulating TAMP as an inference problem on continuous variables to avoid tree search; (b) solving the resulting problem with gradient-based SVGD inference updates using an off-the-shelf differentiable physics simulator; and (c) parallelizing the inference process on the GPU, so that multiple diverse plans can be found in one optimization run.

II. RELATED WORK

Task and Motion Planning Guo et al. [12] categorize TAMP solvers into sampling-based methods [4], [13], [14], [15], [16], [17]; hierarchical methods [18], [19], [20]; constraint-based methods [21], [22], [23]; and optimization-based methods [5], [24], [25]. Our method falls under

¹University of Toronto, ²Carnegie Mellon University, ³NVIDIA, ⁴Massachusetts Institute of Technology, ⁵Technical University of Darmstadt, ⁶McGill University, ⁷University of Sydney. Corresponding author: Yewon Lee (yewonlee@cs.toronto.edu)

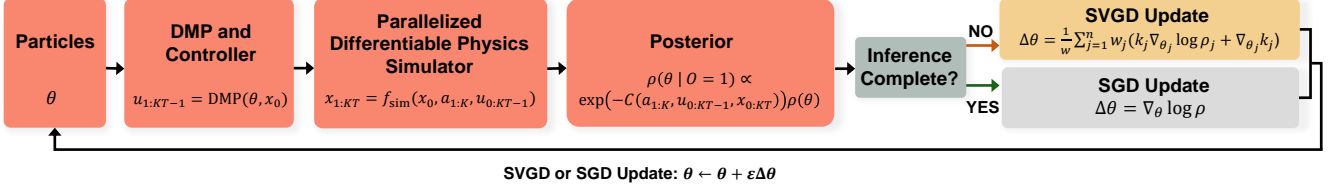


Fig. 2. Overview of STAMP algorithm pipeline. The particles θ represent the task and motion plan $\theta = [a_{1:K}, u_{0:KT-1}]$, or the task plan and a parametrization of the motion plan $\theta = [a_{1:K}, g_{1:K}]$ if Dynamic Movement Primitives dependent on goals $g_{1:K}$ are used (see section IV-B). The resulting controls are passed through a differentiable physics simulator, and particles are updated in parallel using two phases of optimization: an inference phase of SVGD that balances loss minimization with diversification of particles followed by a finetuning phase of SGD so that particles can reach the local optima.

optimization-based methods, which find a complete task and motion plan that optimizes a predefined cost function

Probabilistic Planning Our work is inspired by the idea of approaching planning as inference [26]. Prior works such as [27], [28], [29], [30], [31], [32], [33], [34], [35] have explored the intersection of probability and TAMP. Ha et al. [29] developed probabilistic Logic Geometric Programming (LGP) for solving TAMP in stochastic environments, Shah et al. [27] developed an anytime algorithm for TAMP in stochastic environments, and Kaelbling and Lozano-Pérez extended Hierarchical Planning in the Now [18] to handle current and future state uncertainty. STAMP’s probabilistic interpretation is similar to [29], [36] in that we run inference over a posterior plan distribution, but differs in that our distribution is defined over both discrete and continuous plan parameters rather than over only continuous parameters. While many stochastic TAMP methods can be computationally expensive [12], our method runs efficient, gradient-based inference through parallelization.

Diverse Planning Diverse or top-k symbolic planners like SYM-K and FORBID-K are used to produce sets of feasible task plans [9], [10]. Existing work in TAMP generate different logical plans by adapting diverse symbolic planners, which are iteratively updated with feasibility feedback from the motion planner [6], [8]. Ren et al. [8] rely on a top-k planner to generate a set of candidate logical plans, but only to efficiently find a single TAMP solution rather than a distribution of diverse plans. More similarly to STAMP, Ortiz et al. [6] seek to generate a set of plans based on a novelty criteria, but enforce task diversity by iteratively forbidding paths in the logical planner. In contrast, STAMP finds diverse plans by solving TAMP as an inference problem over plan parameters.

Differentiable Physics Simulation & TAMP Differentiable physics simulators [37], [38], [39], [40], [41], [42], [43], [44] solve a mathematical model of a physical system while allowing the computation of the first-order gradient of the output directly with respect to the parameters or inputs of the system. They have been used to optimize trajectories [40], controls [45], or policies [46]; and for system identification [47], [41]. Toussaint et al. [48] have used differentiable simulation within LGP for sequential manipulation tasks by leveraging simulation gradients for optimization at the path-level. In contrast, STAMP uses simulation gradients to optimize both symbolic and geometric parameters.

Envall et al. [49] used gradient-based optimization for task assignment and motion planning. Their problem formulation

allows task assignments to emerge implicitly in the solution. In contrast, we optimize the task plan explicitly through continuous relaxations, use gradient-based inference to solve TAMP, and obtain gradients from differentiable simulation.

III. PRELIMINARIES

A. Stein Variational Gradient Descent

SVGD is a variational inference algorithm that uses particles to fit a target distribution. Particles are sampled randomly at initialization and updated iteratively until convergence, using gradients of the target distribution with respect to each particle [2]. SVGD is fast, parallelizable, and able to fit both continuous [2] and discrete [3] distributions.

1) *SVGD for Continuous Distributions* [2]: Given a target distribution $p(\theta)$, $\theta \in \mathbb{R}^d$, a randomly initialized set of particles $\{\theta_i\}_{i=1}^n$, a positive definite kernel $k(\theta, \theta')$, and step size ϵ , SVGD iteratively applies the following update rule on $\{\theta_i\}_{i=1}^n$ to approximate the target distribution $p(\theta)$ (where $k_{ji} = k(\theta_j, \theta_i)$ for brevity):

$$\theta_i \leftarrow \theta_i + \frac{\epsilon}{n} \sum_{j=1}^n \underbrace{[\nabla_{\theta_j} \log p(\theta_j) k_{ji}]}_{(A)} + \underbrace{\nabla_{\theta_j} k_{ji}}_{(B)} \quad (1)$$

Term (A), which is a kernel-weighted gradient, encourages the particles to converge towards high-density regions in the target distribution. Term (B) induces a “repulsive force” that prevents all particles from collapsing to a maximum *a posteriori* solution, i.e., it encourages exploration while searching over continuous parameters. This property allows STAMP to find multiple diverse solutions in parallel.

2) *SVGD for Discrete Distributions* [3]: Given a target distribution $p_*(z)$, $z \in \mathcal{Z}$ on a discrete set \mathcal{Z} , SVGD for discrete distributions (DSVGD) introduces relaxations to \mathcal{Z} that reformulates discrete inference as inference on a continuous domain. In our case, z denotes a symbolic/discrete action. To do the relaxation, we construct a differentiable and continuous surrogate distribution $\rho(\theta)$, $\theta \in \mathbb{R}^d$, that approximates the discrete distribution $p_*(z)$. Crucially, a map $\Gamma : \mathbb{R}^d \rightarrow \mathcal{Z}$ is defined such that it divides an arbitrary base distribution $p_0(\theta)$, $\theta \in \mathbb{R}^d$ (e.g., a Gaussian or uniform distribution) into K partitions with equal probability. That is,

$$\int_{\mathbb{R}^d} p_0(\theta) \mathbb{I}[z_i = \Gamma(\theta)] d\theta = 1/K \quad (2)$$

Then, the surrogate distribution $\rho(\theta)$ can be defined as $\rho(\theta) \propto p_0(\theta) \tilde{p}_*(\tilde{\Gamma}(\theta))$ [3], where $\tilde{p}_*(\theta)$, $\theta \in \mathbb{R}^d$ simply denotes

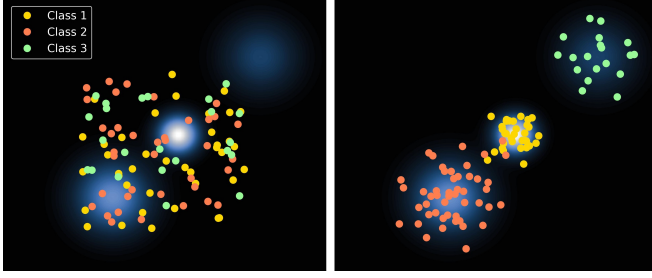


Fig. 3. Fitting a Gaussian mixture with discrete-and-continuous SVGD. Left: random initialization of particles. Right: particles after 500 updates. Note that same-color particles have been assigned to the same mode.

$p_*(z)$, $z \in \mathcal{Z}$ defined on the continuous domain. $\tilde{\Gamma}(\theta)$ is a smooth relaxation of $\Gamma(\theta)$; for instance, $\tilde{\Gamma}(\theta) = \text{softmax}(\theta)$ is a smooth relaxation of $\Gamma(\theta) = \max(\theta)$. After initializing particles $\{\theta_i\}_{i=1}^N$ defined on the continuous domain, DSVG uses the surrogate to update $\{\theta_i\}_{i=1}^N$ via $\theta_i \leftarrow \theta_i + \epsilon \Delta \theta_i$, where $k_{ji} = k(\theta_j, \theta_i)$, $w = \sum_i w_i$, $\rho_j = \rho(\theta_j)$, and:

$$\Delta \theta_i = \sum_{j=1}^n \frac{w_j}{w} (\nabla_{\theta_j} \log \rho_j + \nabla_{\theta_j}) k_{ji}, \quad w_j = \frac{\tilde{p}_*(\tilde{\Gamma}(\theta_j))}{p_*(\Gamma(\theta_j))} \quad (3)$$

Post-convergence, the discrete counterpart of each particle can be recovered by evaluating $\{z_i = \Gamma(\theta_i)\}_{i=1}^N$.

B. Differentiable Physics Simulation

Physics simulators solve the following dynamics equation

$$M\ddot{x} = J^\top f(x, \dot{x}) + C(x, \dot{x}) + \tau(x, \dot{x}, a) \quad (4)$$

to roll out the state (position and orientation) x of the system, subjected to external forces f , Coriolis force C , and joint actuations τ . The Warp simulator [42] used in our paper supports time integration of the above via Semi-Implicit Euler [50] and XPBD [51], [52] schemes and allows fast forward simulations and gradient computations through GPU parallelization. We use the semi-implicit Euler integrator due to its numerical stability [50], [41] and demonstrated success in similar problems [46], [52]. Contacts are resolved in Warp using a spring-based non-penetrative model proposed in [53], [46], while joint limits for articulated bodies are enforced with a spring model following the approach in [46].

Warp computes a forward pass to roll out the system's states $x_{t+1} = f_{\text{sim}}(x_t, \theta_t)$ for all time steps $t = 1, \dots, T$ given control and plan parameters θ_t . Given a loss \mathcal{L} defined on the final or intermediate states, gradients can be backpropagated through the entire trajectory with respect to simulation and plan parameters. As we will explain in following sections, we leverage the differentiability of the simulator to compute the gradients $\nabla_{\theta_j} \log p(\theta_j)$ in term (A) of equation (1).

IV. OUR METHOD: STEIN TASK AND MOTION PLANNING

STAMP solves TAMP as a variational inference problem over discrete symbolic actions and continuous motion plans, conditioned on them being optimal. An analogy to this is trying to sample particles from a known mixture of Gaussians, in which each Gaussian has a distinct class. SVGD must move the particles towards high-density regions in the

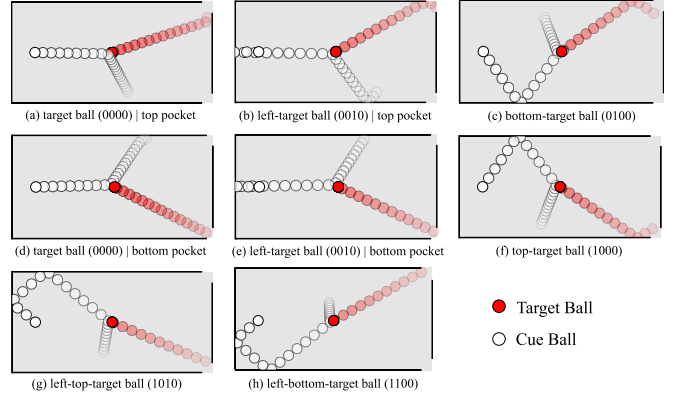


Fig. 4. Sample solutions STAMP found for the billiards problem. Subcaptions indicate which walls the cue ball hits before hitting the target ball. The 1st/2nd/3rd/4th digit correspond to hitting the top/bottom/left/right wall. A 1 means the wall is hit during the shot; a 0 means that it is not. The caption also indicates in which pocket the target ball is shot.

Gaussian (thus learning the continuous parameters) and also learn the correct classes. In TAMP, the Gaussian mixture is analogous to a target distribution where higher likelihood is assigned to optimal solutions, the discrete class is analogous to the discrete task plan, and the continuous parameters are analogous to the motion plan. Figure 3 illustrates how, after SVGD, particles with the same color usually belong to the same Gaussian.

A. Problem Formulation

Given a problem domain, we are interested in sampling optimal symbolic/discrete actions $z_{1:K} \in \mathcal{Z}^K$ and continuous controls $u_{0:KT-1} \in \mathbb{R}^{KT}$ from the posterior

$$p(z_{1:K}, u_{0:KT-1} \mid O = 1) \quad (5)$$

where $O \in \{0, 1\}$ indicates optimality of the plan; K is the number of symbolic action sequences; T is the number of timesteps by which we discretize each action sequence; and \mathcal{Z} is a discrete set of all m possible symbolic actions that can be executed in the domain (i.e., $|\mathcal{Z}| = m$). $z_{1:K}$ and $u_{0:KT-1}$ fully parameterize a task and motion plan, since they can be inputted to a physics simulator f_{sim} along with the initial state x_0 to roll out the system's state at every timestep, that is, $x_{1:KT} = f_{\text{sim}}(x_0, z_{1:K}, u_{0:KT-1})$ ¹.

We use SVGD to sample optimal plans from $p(z_{1:K}, u_{0:KT-1} \mid O = 1)$. As p is defined over both continuous and discrete domains, to use SVGD's gradient-based update rule, we follow Han et al. [3]'s approach and construct a differentiable surrogate distribution for p defined over a continuous domain. We denote this surrogate by ρ .

To construct the surrogate, we first relax the discrete variables by introducing a map from the real domain to \mathcal{Z}^K that evenly partitions some base distribution p_0 . For any problem domain with m symbolic actions, we define $\mathcal{Z} = \{e_i\}_{i=1}^m$ as a collection of m -dimensional one-hot

¹We later introduce $a_{1:K}$, a continuous relaxation of $z_{1:K}$. The forward simulation can also be rolled out using $a_{1:K}$ as $x_{1:KT} = f_{\text{sim}}(x_0, a_{1:K}, u_{0:KT-1})$, which will ensure gradients can be taken with respect to $a_{1:K}$. This is important as $z_{1:K}$ is discrete.

vectors². Then, $z_{1:K} \in \mathcal{Z}^K$, implying that we commit to one action (e_i) in each of the K action phases. Further, we use a uniform distribution for the base distribution p_0 . Given this formulation, we can define our map³ $\Gamma : \mathbb{R}^{mK} \rightarrow \mathcal{Z}^K$ and its differentiable surrogate $\tilde{\Gamma}$ as the following:

$$\begin{aligned}\Gamma(a_{1:K}) &= [\max\{a_1\} \dots \max\{a_K\}]^\top = z_{1:K} \\ \tilde{\Gamma}(a_{1:K}) &= [\text{softmax}\{a_1\} \dots \text{softmax}\{a_K\}]^\top = \tilde{z}_{1:K}.\end{aligned}\quad (6)$$

We show in Appendix VIII that the above map indeed partitions p_0 evenly when p_0 is the uniform distribution.

By constructing the above map, we can run inference over purely continuous variables $a_{1:K} \in \mathbb{R}^{mK}$ and $u_{0:KT-1} \in \mathbb{R}^{KT-1}$ and recover the discrete plan parameters post-inference via $z_{1:K} = \Gamma(a_{1:K})$. We denote $a_{1:K} \in \mathbb{R}^{mK}$ and $u_{0:KT-1} \in \mathbb{R}^{KT-1}$ collectively as a particle, that is, $\theta = [a_{1:K}, u_{0:KT-1}]^\top$, and randomly initialize $\{\theta_i\}_{i=1}^n$ to run SVGD inference. The target distribution we aim to infer is a differentiable surrogate ρ of the posterior p defined as:

$$\rho(a_{1:K}, u_{0:KT-1} \mid O = 1) \quad (7)$$

$$\propto p_0(a_{1:K}) p(\tilde{\Gamma}(a_{1:K}), u_{0:KT-1} \mid O = 1). \quad (8)$$

In practice, because $p_0(a_{1:K})$ can be treated as a constant by making its boundary arbitrarily large (see Appendix VIII-A), we simply remove p_0 from the expression above.

Note that it is not necessary to normalize the ρ as the normalization constant vanishes by taking the gradient of $\log \rho$ in the SVGD updates. We now quantify the surrogate of the posterior distribution. We begin by applying Bayes' rule and obtain the following factorization of $\rho(\theta \mid O = 1)$:

$$\rho(\theta \mid O = 1) \propto p(O = 1 \mid \theta) p(\theta) \quad (9)$$

Since the likelihood function is synonymous with a plan's optimality, we formulate the likelihood via the total cost C associated with the relaxed task and motion plan θ :

$$p(O = 1 \mid \theta) \propto \exp\{-C(\theta, x_{0:KT})\} \quad (10)$$

Meanwhile, the prior $p(\theta)$ is defined over θ only and as such, we use it to impose constraints on the plan parameters (e.g., kinematic constraints on robot joints).

Related to the logic-geometric programming (LGP) [48], [54], [55], [5], [29] framework, which optimizes a cost subject to constraint functions that activate or deactivate when kinematic/logical action transition events occur, $C(\theta)$ in our method is a sum of *relaxed* versions of both the cost and constraint functions. Here, "relaxed" refers to removing the cost and constraints' dependence on the discrete logical variables through our relaxations, and defining costs/constraint functions that are differentiable w.r.t. our plan parameters θ .

B. Problem Reduction Using Motion Primitives

Rather than running inference over $\theta = [a_{1:K}, u_{0:KT-1}]^\top$, we can also reduce the dimensionality of θ using a bank of

²The i th element of e_i is 1 and all other elements are 0.

³Given $a_k \in \mathbb{R}^m$, $\max\{a_k\}$ returns a m -dimensional one-hot encoding e_i iff the i th element of a_k is the larger than all other elements.

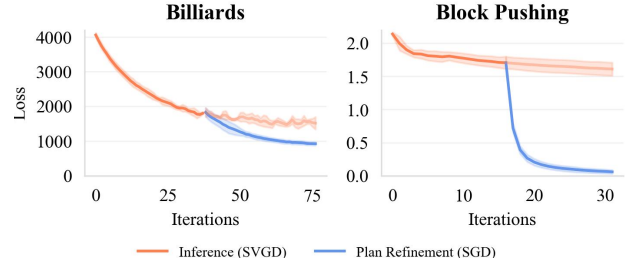


Fig. 5. Evolution of mean cost over all particles averaged across 5 runs.

goal-conditioned dynamic motion primitives (DMP)s (more details in Appendix IX-B). We redefine the particle to be $\theta = [a_{1:K}, g_{1:K}]^\top$, where $g_{1:K} \in \mathbb{R}^{Kd}$ denotes goal poses for the system after executing action k , and d is the DOF of the system. With just g_k , we recover the full trajectory $x_{0:KT-1}$ by integrating the system of equations in (36) and computing the controls $u_{0:KT-1}$ using a simple trajectory tracking controller. Note that to do this, we train a bank of goal-conditioned DMPs from demonstration data for every action offline. This new inference problem over $[a_{1:K}, g_{1:K}]^\top$ is more tractable than the original inference problem over $[a_{1:K}, u_{0:KT-1}]^\top$ due to the reduced dimensionality.

C. STAMP Algorithm

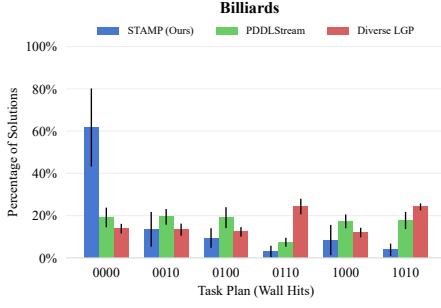
Given a problem domain with cost $C(\theta)$ and n randomly initialized particles $\theta = \{\theta_i\}_{i=1}^n$, STAMP finds a distribution of optimal solutions to the inference problem $\rho(\theta \mid O = 1)$ by running SVGD inference until convergence and subsequently refining the plans via SGD updates. During SVGD, each of the n plans (θ) are executed and simulated in Warp. After obtaining states $x_{0:KT} = f_{\text{sim}}(x_0, a_{1:K}, u_{0:KT-1})$ for each particle, the posterior distribution and its surrogate are computed using equations (5) and (7). Gradients of the log-posterior with respect to $\{\theta_i\}_{i=1}^n$ are obtained via Warp's auto-differentiation capabilities, and these gradients are used to update each candidate plan θ_i via update rule (3). During stochastic gradient descent (SGD), the above steps are repeated except for the update rule, which changes to $\theta \leftarrow \theta + \epsilon \nabla_{\theta} \log \rho$. Switching to SGD after SVGD allows us to finetune our plans, as the repulsive term $\nabla_{\theta} k(\theta, \theta')$ in SVGD can push the plans away from optima, but with SGD the plans are optimized to reach them. All of the above computations (physics simulations, log posterior evaluations, and gradient computations for all particles) are run in parallel on the GPU, making STAMP highly efficient. Figure 2 shows the algorithm pipeline and Algorithm 1 shows the pseudocode.

V. EVALUATION

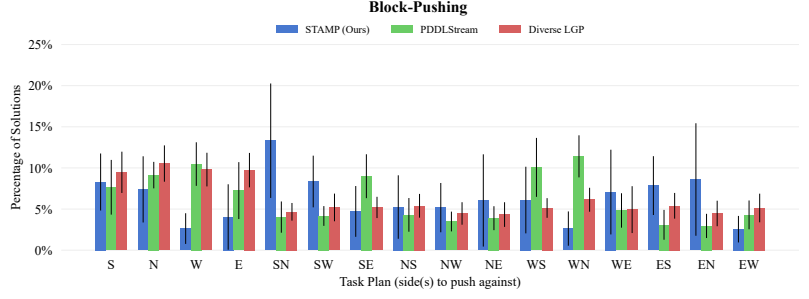
We run STAMP on three problems: billiards, block-pushing, and pick-and-place. We benchmark STAMP against two TAMP baselines that build upon PDDLStream [4] and Diverse LGP [6] (implementation details are in Appendix XIV).

A. Problem Environments and Their Algorithmic Setup

1) *Billiards*: The goal is to optimize the initial velocity u_0 on the cue ball that sends the target ball into one of the two pockets in Figure 8. This requires planning on the



(a) STAMP found 104 solutions in (6.94 ± 0.06) s. Diverse LGP and PDDLStream are invoked 104 times.



(b) STAMP found 825 solutions in (12.92 ± 0.04) s. Diverse LGP and PDDLStream are invoked 150 times.

Fig. 6. Distribution of plans found by STAMP (our method), Diverse LGP, and PDDLStream. Results are averages across 10 seeds; error bars represents standard deviation. Solutions for the remaining modes (not shown) were not found by any method.

continuous domain ($u_0 \in \mathbb{R}^2$) and discrete domain (the set of walls we wish for the cue ball to hit before colliding with the target ball). We define our particles as $\theta = [u_0, z]$ where $z = [z_1, z_2, z_3, z_4] \in \{0, 1\}^4$, which indicates which of the four walls the cue ball bounces off of.⁴ The cost function C is a weighted sum of the target loss L_{target} and aim loss L_{aim} , which are minimal when the cue ball ends up in either of the two pockets if the cue ball comes in contact with the target ball at any point in its trajectory, respectively. Hyperparameters $\beta_{\text{target}}, \beta_{\text{aim}} > 0$ are the loss' respective coefficients:

$$C(\theta) = \beta_{\text{aim}} L_{\text{aim}} + \beta_{\text{target}} L_{\text{target}} \quad (11)$$

Appendix X provides additional details on the problem setup.

2) *Block-Pushing*: The goal is to push the block in Figure 9 towards the goal region. The symbolic plan is the sequence of sides (north, east, south, west) to push against. Assuming *a priori* that up to K action sequences can be committed, we define the particles as $\theta = [a_1, \dots, a_K, g_1, \dots, g_K]^T$, where $a_k \in \mathbb{R}^4$ are the relaxed symbolic variables and $g_k = [g_k^x, g_k^y, g_k^{\phi}] \in \mathbb{R}^3$ denote individual goal poses after executing each action. Given the goals, we use pretrained DMPs to obtain trajectories and control inputs. The discrete task variable for the k th action can be recovered via equation (6). The cost is the weighted sum of the target loss L_{target} and trajectory loss L_{traj} . L_{target} penalizes large distances between the cube and the goal region at the final time-step.

$$C(\theta) = \beta_{\text{target}} L_{\text{target}}(x_{KT}) + \beta_{\text{traj}} L_{\text{traj}}(g_{1:K}^{x,y}) \quad (12)$$

Appendix XI provides further details on the problem setup.

3) *Pick-and-Place*: Using an end effector, the goal is to pick and place blocks 1, 2, and 3 such that block 1 ends up in one of two targets shown in Figure 10. Long horizon reasoning is required in this problem, as blocks 2 and 3 occlude the targets; hence, either block 2 or 3 have to be moved out of the way before block 1 can be placed. Our goal can be expressed as

$$((\text{cube1} \in \mathcal{A}) \vee (\text{cube1} \in \mathcal{B})) \quad (13)$$

$$\wedge \neg \text{onTop}(\text{cube1}, \text{cube2}) \wedge \neg \text{onTop}(\text{cube1}, \text{cube3})$$

Symbolic actions are $\mathcal{Z} = \{\text{pick}(\text{cube}), \text{place}(\text{cube})\} \forall \text{cube} \in \mathcal{C}$ (where $\mathcal{C} = \{\text{cube1}, \text{cube3}, \text{cube3}\}$) which are represented numerically via one-hot encodings as discussed in Section IV-A. Particles are defined as $\theta = [a_1, \dots, a_K, g_1, \dots, g_K]^T$, where $a_{1:K}$ represent which K -length sequence of symbolic actions are executed, and $g_{1:K}$ represent the intermediate goal poses of the end effector after executing each action.

Unlike in previous examples, the symbolic actions have preconditions and postconditions which constitute constraints in our problem. For each pre/postcondition, we construct differentiable loss functions $L_{\text{pre}(\cdot)}, L_{\text{post}(\cdot)} \geq 0$ that are minimal when the condition is met. The constraint associated with action $z \in \mathcal{Z}$ is then expressed as the γ_i - and γ_j -weighted sum of its precondition losses and postcondition losses, where $\gamma_i, \gamma_j > 0$ are scalar hyperparameters:

$$L_z(x_{t_0:t_T}) = \sum_{i \in \text{pre}(z)} \gamma_i L_i(x_{t_0}, g) + \sum_{j \in \text{post}(z)} \gamma_j L_j(x_{t_T}) \quad (14)$$

Please see Appendix XII-B for more details on the pre/postcondition losses for each action.

We optimize towards the logical goal stated in (V-A.3) by defining the total target loss as the sum of each cube's individual target loss weighted by a soft indicator function ω_c that gets activated when the cube is held (see Appendix XII-C). The target loss of cube c , $L_{\text{target},c}$, and its gradient will dominate the optimization if c is held by the gripper, which is a necessary condition for placing c in its target.

$$L_{\text{target}}(x_{t_0}, x_{t_T}) = \sum_{c \in \mathcal{C}} \omega_c(x_{t_0}) \cdot L_{\text{target},c}(x_{t_T}). \quad (15)$$

The target loss for each cube is defined in Appendix XII-D.

Finally, the total cost function is constructed as a sum over all constraints $\mathbf{L}_z(x_{t_0:t_T}) = [L_z(x_{t_0:t_T}) \forall z \in \mathcal{Z}]^T$ weighted by $\tilde{z}_k = \tilde{\Gamma}(a_k) \forall k = 1, \dots, K$ and the target loss, which is computed after executing each action⁵.

$$C(\theta) = \sum_{k=1}^K \left(\tilde{z}_k \cdot \mathbf{L}_z(x_{(k-1)T+1:kT}) + L_{\text{target}}(x_{kT}) \right) \quad (16)$$

⁵Recall that K is the number of action sequences, a_k the component of the particle representing the task plan, and $\tilde{\Gamma}(\cdot)$ a composition of softmax operations.

⁴ $z_i = 1$ if the cue ball hits wall i , and it is 0 otherwise.

TABLE I
STAMP’S RUNTIME VS. BASELINES

	Method	Time / Solution (s)		Runtime (s)
Billiards	Diverse LGP	7.5	± 0.9	7.5 ± 0.9
	PDDLStream	5.7	± 0.8	5.7 ± 0.8
	STAMP (Ours)	0.068	± 0.007	6.94 ± 0.06
Pusher	Diverse LGP	22.6	± 7.6	22.6 ± 7.6
	PDDLStream	22.2	± 0.1	110.9 ± 0.7
	STAMP (Ours)	0.0157	± 0.0004	12.92 ± 0.04

Averaged across 10 seeds; 1100 particles; max. 2 pushes.

TABLE II
STAMP’S RUNTIME VARYING THE
NUMBER OF PARTICLES

#Particles	Billiards (s)	Pusher (s)
700	6.30 ± 0.07	12.53 ± 0.05
900	6.55 ± 0.04	12.74 ± 0.03
1100	6.94 ± 0.06	12.92 ± 0.04
1300	7.71 ± 0.12	13.22 ± 0.06

Averaged across 10 seeds; max. 2 pushes.

TABLE III
STAMP’S RUNTIME VARYING THE
PARTICLE DIMENSIONALITY (PUSHER)

Max. #Pushes	Dim.	Runtime (s)
2	16	12.92 ± 0.04
3	24	12.93 ± 0.04
4	32	13.26 ± 0.03
5	40	13.57 ± 0.03

Averaged across 10 seeds; 1100 particles.

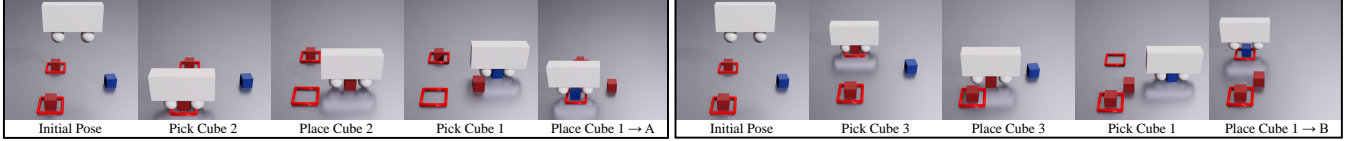


Fig. 7. Both solutions for the pick and place experiment obtained simultaneously from running STAMP. See Figure 10 for the experiment setup. The left solution removes Cube 2 to place Cube 1 in target A. The right solution removes Cube 3 to place Cube 1 in target B.

The global optima of $C(\theta)$ are thus action sequences $z_{1:K} = \Gamma(a_{1:K})$ and intermediate goal poses that solve the goal while ensuring all pre/postconditions are met. Further, C is amenable to gradient-based methods like STAMP since it is differentiable w.r.t. both $a_{1:K}$ and $g_{1:K}$. Note that because of the construction of $C(\theta)$ as a sum over k , STAMP can be run for each k separately (see Appendix XII-F), diminishing the need to take gradients through the entire trajectory $x_{0:KT}$, which may be prone to exploding gradients.

B. Experimental Results (Simulation)

We investigate the following questions:

- (Q1) Can STAMP return a variety of plans to problems for which multiple solutions are possible?
- (Q2) How does STAMP’s runtime compare to search-based TAMP baselines?
- (Q3) How does STAMP’s runtime scale w.r.t. problem dimensionality and number of particles?
- (Q4) Is SGD necessary in STAMP to find optimal plans?

1) *Solution Diversity*: STAMP finds a variety of solutions to all three problems; Figures 4, 12, and 7 show sample solutions. While STAMP finds a distribution of solutions in a single run, baseline methods can only find one solution per run. In Figures 6a and 6b, we show a histogram of solutions STAMP found in one run compared to solutions found using baseline methods by invoking them multiple times.

2) *Runtime Efficiency*: STAMP produces large plan sets in substantially less time than the baselines. Table I shows that the time it takes STAMP to generate hundreds of solutions is often less than the time needed for Diverse LGP [6] and PDDLStream [4] baselines to produce a single solution.

3) *Scalability to Higher Dimensions and Greater Number of Particles*: Tables II and III show the total runtime of our algorithm while varying the number of particles and particle dimensions. Increasing the number of particles and the dimensions of the particles has little effect on the total optimization time, which is consistent with expectations as our method is parallelized over the GPU.⁶

⁶GPU parallelization is made possible through the use of SVGD, a parallelizable inference algorithm, and the Warp simulator.

4) *SGD Plan Refinement*: Figure 5 shows the cost evolution with SGD plan refinement versus solely using SVGD for the same number of iterations. Pure SVGD inference results in slow or poor convergence, while running SGD post-SVGD inference results in better convergence.

C. Experimental Results (Real Robot)

We demonstrate STAMP on a real robot system using a front-view camera, AprilTags [56] for pose estimation of cube(s) and target(s), and a Franka Emika Panda robotic arm. We input the detected poses into STAMP and track the resulting trajectory directly. For the block pushing experiment, we vary the cube and target positions across 3 distinct configurations and set the end-effector to follow the pose of one of the block’s faces. While several trajectories returned by STAMP involve rotations that are infeasible due to differences in real world friction, the lowest loss solution in the most popular 3-5 modes of each problem setup successfully solve the problem, as shown in Figure 1. More real world experiments and videos can be found on our [project website](#).

VI. CONCLUSION

We introduced STAMP, a novel algorithm that approaches TAMP as a variational inference problem over discrete symbolic action and continuous motion parameters. STAMP solves the inference problem using SVGD and gradients from differentiable simulation. We validated our approach on the billiards, block-pushing, and pick-and-place problems, where STAMP was able to discover a diverse set of plans covering multiple different task sequences and motion plans. STAMP, through exploiting parallel gradient computation from a differentiable simulator, is much faster at finding a variety of solutions than baselines, and its runtime scales well to higher dimensions and more particles.

VII. ACKNOWLEDGEMENTS

YL was supported by the Google DeepMind Fellowship, NSERC Canada Graduate Scholarship, and Ontario Graduate Scholarship. This article solely reflects the opinions and conclusions of its authors and not the sponsors.

REFERENCES

- [1] C. R. Garrett, R. Chitnis, R. Holladay, B. Kim, T. Silver, L. P. Kaelbling, and T. Lozano-Pérez, “Integrated task and motion planning,” *Annual review of control, robotics, and autonomous systems*, vol. 4, pp. 265–293, 2021.
- [2] Q. Liu and D. Wang, “Stein variational gradient descent: A general purpose bayesian inference algorithm,” in *Advances in Neural Information Processing Systems*, D. Lee, M. Sugiyama, U. Luxburg, I. Guyon, and R. Garnett, Eds., vol. 29. Curran Associates, Inc., 2016.
- [3] J. Han, F. Ding, X. Liu, L. Torresani, J. Peng, and Q. Liu, “Stein variational inference for discrete distributions,” in *AISTATS*. PMLR, 2020, pp. 4563–4572.
- [4] C. R. Garrett, T. Lozano-Pérez, and L. P. Kaelbling, “PDDLStream: Integrating symbolic planners and blackbox samplers via optimistic adaptive planning,” *ICAPS*, vol. 30, pp. 440–448, Jun. 2020.
- [5] M. Toussaint, “Logic-Geometric programming: An Optimization-Based approach to combined task and motion planning,” in *Twenty-Fourth International Joint Conference on Artificial Intelligence*, Jun. 2015.
- [6] J. Ortiz-Haro, E. Karpas, M. Toussaint, and M. Katz, “Conflict-directed diverse planning for logic-geometric programming,” *Proceedings of the International Conference on Automated Planning and Scheduling*, vol. 32, no. 1, pp. 279–287, 6 2022.
- [7] T. Ren, G. Chalvatzaki, and J. Peters, “Extended task and motion planning of long-horizon robot manipulation,” *arXiv preprint arXiv:2103.05456*, 2021.
- [8] —, “Extended tree search for robot task and motion planning,” *arXiv preprint arXiv:2103.05456*, 2021.
- [9] D. Speck, R. Mattmüller, and B. Nebel, “Symbolic top-k planning,” in *Proceedings of the Thirty-Fourth AAAI Conference on Artificial Intelligence (AAAI 2020)*, V. Conitzer and F. Sha, Eds. AAAI Press, 2020, pp. 9967–9974.
- [10] M. Katz, S. Sohrabi, O. Udrea, and D. Winterer, “A novel iterative approach to top-k planning,” in *Proceedings of the Twenty-Eighth International Conference on Automated Planning and Scheduling (ICAPS 2018)*. AAAI Press, 2018, pp. 132–140.
- [11] M. Dalal, A. Mandlekar, C. Garrett, A. Handa, R. Salakhutdinov, and D. Fox, “Imitating task and motion planning with visuomotor transformers,” *Conference on Robot Learning*, 2023.
- [12] H. Guo, F. Wu, Y. Qin, R. Li, K. Li, and K. Li, “Recent trends in task and motion planning for robotics: A survey,” *ACM Computing Surveys*, 2023.
- [13] C. R. Garrett, T. Lozano-Pérez, and L. P. Kaelbling, “Ffrob: Leveraging symbolic planning for efficient task and motion planning,” *The International Journal of Robotics Research*, vol. 37, no. 1, pp. 104–136, 2018.
- [14] C. R. Garrett, T. Lozano-Pérez, and L. P. Kaelbling, “Sampling-based methods for factored task and motion planning,” *The International Journal of Robotics Research*, vol. 37, no. 13-14, pp. 1796–1825, 2018.
- [15] —, “Stripstream: Integrating symbolic planners and blackbox samplers,” *ICAPS Workshop on Planning and Robotics (PlanRob)*, 2018.
- [16] —, “Pddlstream: Integrating symbolic planners and blackbox samplers via optimistic adaptive planning,” in *Proceedings of the International Conference on Automated Planning and Scheduling*, vol. 30, 2020, pp. 440–448.
- [17] W. Thomason and R. A. Knepper, “A unified sampling-based approach to integrated task and motion planning,” in *The International Symposium of Robotics Research*. Springer, 2019, pp. 773–788.
- [18] L. P. Kaelbling and T. Lozano-Pérez, “Hierarchical task and motion planning in the now,” in *2011 IEEE International Conference on Robotics and Automation*, May 2011, p. 1470–1477.
- [19] L. P. Kaelbling and T. Lozano-Pérez, “Integrated task and motion planning in belief space,” *International Journal of Robotics Research*, vol. 32, no. 9-10, pp. 1194–1227, Aug. 2013.
- [20] A. Suárez-Hernández, G. Alenyà, and C. Torras, “Interleaving hierarchical task planning and motion constraint testing for dual-arm manipulation,” in *2018 IEEE/RSJ International Conference on Intelligent Robots and Systems (IROS)*. IEEE, 2018, pp. 4061–4066.
- [21] N. T. Dantam, Z. K. Kingston, S. Chaudhuri, and L. E. Kavraki, “Incremental task and motion planning: A constraint-based approach,” in *Robotics: Science and systems*, vol. 12. Ann Arbor, MI, USA, 2016, p. 00052.
- [22] —, “An incremental constraint-based framework for task and motion planning,” *The International Journal of Robotics Research*, vol. 37, no. 10, pp. 1134–1151, 2018.
- [23] K. He, M. Lahijanian, L. E. Kavraki, and M. Y. Vardi, “Towards manipulation planning with temporal logic specifications,” in *2015 IEEE international conference on robotics and automation (ICRA)*. IEEE, 2015, pp. 346–352.
- [24] C. Zhang and J. A. Shah, “Co-optimizing task and motion planning,” in *2016 IEEE/RSJ International Conference on Intelligent Robots and Systems (IROS)*. IEEE, 2016, pp. 4750–4756.
- [25] S. Saha and A. A. Julius, “Task and motion planning for manipulator arms with metric temporal logic specifications,” *IEEE robotics and automation letters*, vol. 3, no. 1, pp. 379–386, 2017.
- [26] M. Botvinick and M. Toussaint, “Planning as inference,” *Trends in cognitive sciences*, vol. 16, no. 10, pp. 485–488, 2012.
- [27] N. Shah, D. K. Vasudevan, K. Kumar, P. Kamoghajala, and S. Srivastava, “Anytime integrated task and motion policies for stochastic environments,” in *2020 IEEE International Conference on Robotics and Automation (ICRA)*. IEEE, 2020, pp. 9285–9291.
- [28] L. P. Kaelbling and T. Lozano-Pérez, “Integrated task and motion planning in belief space,” *The International Journal of Robotics Research*, vol. 32, no. 9-10, pp. 1194–1227, 2013.
- [29] J.-S. Ha, D. Driess, and M. Toussaint, “A probabilistic framework for constrained manipulations and task and motion planning under uncertainty,” in *2020 IEEE International Conference on Robotics and Automation (ICRA)*, May 2020, pp. 6745–6751.
- [30] I. A. Şucan and L. E. Kavraki, “Accounting for uncertainty in simultaneous task and motion planning using task motion multigraphs,” in *2012 IEEE International Conference on Robotics and Automation*. IEEE, 2012, pp. 4822–4828.
- [31] W. Zhao and W. Chen, “Hierarchical pomdp planning for object manipulation in clutter,” *Robotics and Autonomous Systems*, vol. 139, p. 103736, 2021.
- [32] L. Kaelbling and T. Lozano-Pérez, “Domain and plan representation for task and motion planning in uncertain domains,” in *IROS Workshop on Knowledge Representation for Autonomous Robots*, 2011.
- [33] D. Hadfield-Menell, E. Groshev, R. Chitnis, and P. Abbeel, “Modular task and motion planning in belief space,” in *2015 IEEE/RSJ International Conference on Intelligent Robots and Systems (IROS)*. IEEE, 2015, pp. 4991–4998.
- [34] M. Hou, T. X. Lin, H. Zhou, W. Zhang, C. R. Edwards, and F. Zhang, “Belief space partitioning for symbolic motion planning,” in *2021 IEEE International Conference on Robotics and Automation (ICRA)*. IEEE, 2021, pp. 8245–8251.
- [35] C. R. Garrett, C. Paxton, T. Lozano-Pérez, L. P. Kaelbling, and D. Fox, “Online replanning in belief space for partially observable task and motion problems,” in *2020 IEEE International Conference on Robotics and Automation (ICRA)*. IEEE, 2020, pp. 5678–5684.
- [36] A. Lambert, A. Fishman, D. Fox, B. Boots, and F. Ramos, “Stein variational model predictive control,” *Conference on Robot Learning (CoRL)*, 2020.
- [37] F. de Avila Belbute-Peres, K. Smith, K. Allen, J. Tenenbaum, and J. Z. Kolter, “End-to-end differentiable physics for learning and control,” *32nd Conference on Neural Information Processing Systems (NeurIPS)*, vol. 31, 2018.
- [38] Y.-L. Qiao, J. Liang, V. Koltun, and M. C. Lin, “Scalable differentiable physics for learning and control,” *Proceedings of the 37th International Conference on Machine Learning (ICML)*, 2020.
- [39] K. Werling, D. Omens, J. Lee, I. Exarchos, and K. Liu, “Fast and Feature-Complete differentiable physics engine for articulated rigid bodies with contact constraints,” *Robotics: Science and Systems XVII*, 2021.
- [40] T. A. Howell, S. Le Cleac’h, J. Z. Kolter, M. Schwager, and Z. Manchester, “Dojo: A differentiable simulator for robotics,” *arXiv preprint arXiv:2203.00806*, vol. 9, 2022.
- [41] J. K. Murthy, M. Macklin, F. Golemo, V. Voleti, L. Petrini, M. Weiss, B. Considine, J. Parent-Lévesque, K. Xie, K. Erleben, L. Paull, F. Shkurti, D. Nowrouzezahrai, and S. Fidler, “gradsim: Differentiable simulation for system identification and visuomotor control,” in *International Conference on Learning Representations*, 2021.
- [42] M. Macklin, “Warp: A high-performance python framework for gpu simulation and graphics,” <https://github.com/nvidia/warp>, 3 2022, nVIDIA GPU Technology Conference (GTC).
- [43] C. D. Freeman, E. Frey, A. Raichuk, S. Girgin, I. Mordatch, and O. Bachem, “Brax—a differentiable physics engine for large scale rigid body simulation,” *35th Conference on Neural Information Processing Systems (NeurIPS 2021) Track on Datasets and Benchmarks*, 2021.

- [44] Y. Hu, L. Anderson, T.-M. Li, Q. Sun, N. Carr, J. Ragan-Kelley, and F. Durand, “DiffTaichi: Differentiable programming for physical simulation,” *International Conference on Learning Representations (ICLR)*, 2020.
- [45] E. Heiden, M. Macklin, Y. Narang, D. Fox, A. Garg, and F. Ramos, “Disect: A differentiable simulation engine for autonomous robotic cutting,” *Robotics: Science and Systems*, 2021.
- [46] J. Xu, V. Makovychuk, Y. Narang, F. Ramos, W. Matusik, A. Garg, and M. Macklin, “Accelerated policy learning with parallel differentiable simulation,” *International Conference on Learning Representations (ICLR)*, 2022.
- [47] E. Heiden, C. E. Denniston, D. Millard, F. Ramos, and G. S. Sukhatme, “Probabilistic inference of simulation parameters via parallel differentiable simulation,” in *2022 International Conference on Robotics and Automation (ICRA)*, 2022, pp. 3638–3645.
- [48] M. Toussaint, K. Allen, K. Smith, and J. Tenenbaum, “Differentiable physics and stable modes for Tool-Use and manipulation planning,” *Robotics: Science and Systems XIV*, 2018.
- [49] J. Envall, R. Poranne, and S. Coros, “Differentiable task assignment and motion planning,” *IEEE/RSJ International Conference on Intelligent Robots and Systems (IROS)*, 2023.
- [50] T. Erez, Y. Tassa, and E. Todorov, “Simulation tools for model-based robotics: Comparison of bullet, havok, mujoco, ode and physx,” in *2015 IEEE international conference on robotics and automation (ICRA)*. IEEE, 2015, pp. 4397–4404.
- [51] M. Macklin, M. Müller, and N. Chentanez, “Xpbd: position-based simulation of compliant constrained dynamics,” in *Proceedings of the 9th International Conference on Motion in Games*, 2016, pp. 49–54.
- [52] M. Macklin, K. Storey, M. Lu, P. Terdiman, N. Chentanez, S. Jeschke, and M. Müller, “Small steps in physics simulation,” in *Proceedings of the 18th Annual ACM SIGGRAPH/Eurographics Symposium on Computer Animation*, 2019, pp. 1–7.
- [53] J. Xu, T. Chen, L. Zlokapa, M. Foshey, W. Matusik, S. Sueda, and P. Agrawal, “An end-to-end differentiable framework for contact-aware robot design,” *Robotics: Science and Systems*, 2021.
- [54] D. Driess, J.-S. Ha, M. Toussaint, and R. Tedrake, “Learning models as functionals of Signed-Distance fields for manipulation planning,” in *Proceedings of the 5th Conference on Robot Learning*, ser. Proceedings of Machine Learning Research, A. Faust, D. Hsu, and G. Neumann, Eds., vol. 164. PMLR, 2022, pp. 245–255.
- [55] M. Toussaint, J.-S. Ha, and D. Driess, “Describing physics for physical reasoning: Force-Based sequential manipulation planning,” *IEEE Robotics and Automation Letters*, vol. 5, no. 4, pp. 6209–6216, Oct. 2020.
- [56] E. Olson, “Apriltag: A robust and flexible visual fiducial system,” in *2011 IEEE International Conference on Robotics and Automation*, May 2011, p. 3400–3407. [Online]. Available: <https://ieeexplore.ieee.org/document/5979561>
- [57] P. Pastor, H. Hoffmann, T. Asfour, and S. Schaal, “Learning and generalization of motor skills by learning from demonstration,” in *2009 IEEE International Conference on Robotics and Automation*, May 2009, pp. 763–768.
- [58] D.-H. Park, H. Hoffmann, P. Pastor, and S. Schaal, “Movement reproduction and obstacle avoidance with dynamic movement primitives and potential fields,” *Humanoids 2008 - 8th IEEE-RAS International Conference on Humanoid Robots*, pp. 91–98, 2008.
- [59] H. Tan, E. Erdemir, K. Kawamura, and Q. Du, “A potential field method-based extension of the dynamic movement primitive algorithm for imitation learning with obstacle avoidance,” *2011 IEEE International Conference on Mechatronics and Automation*, pp. 525–530, 2011.
- [60] M. Ginesi, D. Meli, A. Roberti, N. Sansonetto, and P. Fiorini, “Dynamic movement primitives: Volumetric obstacle avoidance using dynamic potential functions,” *Journal of Intelligent & Robotic Systems*, vol. 101, 2020.
- [61] D. Garreau, W. Jitkrittum, and M. Kanagawa, “Large sample analysis of the median heuristic,” *arXiv preprint arXiv:1707.07269*, 2017.
- [62] C. Bäckström and B. Nebel, “Complexity results for sas+ planning,” *Computational Intelligence*, vol. 11, no. 4, pp. 625–655, 1995.
- [63] S. Richter and M. Westphal, “The lama planner: Guiding cost-based anytime planning with landmarks,” *Journal of Artificial Intelligence Research*, vol. 39, pp. 127–177, 2010.
- [64] M. Helmert, “The fast downward planning system,” *Journal of Artificial Intelligence Research*, vol. 26, pp. 191–246, 7 2006.

VIII. RELAXATIONS FOR DISCRETE SVGD

Given a problem domain with m possible actions, the goal of TAMP is to find a K -length sequence of symbolic actions $z_{1:K} \in \mathcal{Z}^K$ and associated motions that solve some goal. Here, \mathcal{Z} is a discrete set of m possible symbolic actions in the domain. We propose the general formulation of \mathcal{Z} as the set of m -dimensional one-hot encodings such that $|\mathcal{Z}| = m$ and $|\mathcal{Z}^K| = m^K$. Then, as per equation (2), we can simply relax $z_{1:K} \in \mathcal{Z}^K$ to the real domain \mathbb{R}^{mK} by constructing the map $\Gamma : \mathbb{R}^{mK} \rightarrow \mathcal{Z}^K$ as

$$\Gamma(a_{1:K}) = \begin{bmatrix} \max\{a_1\} \\ \max\{a_2\} \\ \vdots \\ \max\{a_K\} \end{bmatrix} \quad (17)$$

and its differentiable surrogate as

$$\tilde{\Gamma}(\cdot) = \begin{bmatrix} \text{softmax}\{a_1\} \\ \text{softmax}\{a_2\} \\ \vdots \\ \text{softmax}\{a_K\} \end{bmatrix}. \quad (18)$$

We will prove that the above mapping evenly partitions \mathbb{R}^{mK} into m^K parts when the base distribution p_0 is a uniform distribution over $[-u, u]^{mK}$ for some $u > 0$. We will prove this in two steps: firstly by assuming $K = 1$ and then proving this for any positive integer K .

A. The Base Distribution

Our base distribution $p_0(\theta)$, $\theta \in \mathbb{R}^{mK}$ for discrete SVGD is a uniform distribution over the domain $[-u, u]^{mK}$. That is,

$$p_0(\theta) = \text{unif}(\theta) = \begin{cases} \frac{1}{(2u)^{mK}} & \text{if } \theta \in [-u, u]^{mK} \\ 0 & \text{otherwise.} \end{cases} \quad (19)$$

Note that in practice, we can make $u \in (0, \infty)$ arbitrarily large to avoid taking gradients of p_0 at the boundaries of $[-u, u]^K$.

B. Proof of Even Partitioning: Case $K = 1$

To satisfy the condition that $\Gamma(\theta)$, $\theta \in \mathbb{R}^m$ evenly partitions $\text{unif}(\theta)$, for all $\{e_i\}_{i=1}^m \in \mathcal{Z}$, the following must be true.

$$\int_{\mathbb{R}^m} \text{unif}(\theta) \mathbb{I}[e_i = \Gamma(\theta)] d\theta = \frac{1}{m} \quad (20)$$

Below, we show that the left hand side (LHS) of the above equation simplifies to $\frac{1}{m}$, proving that our relaxation evenly

partitions $p_0(\cdot)$.

$$\text{LHS} = \int_{\mathbb{R}^m} \text{unif}(\theta) \mathbb{I}[e_i = \max(\theta)] d\theta \quad (21)$$

$$= \frac{1}{(2u)^m} \int_{-u}^u \dots \int_{-u}^u \mathbb{I}[e_i = \max(\theta)] dx_1 \dots dx_m \quad (22)$$

$$= \frac{1}{(2u)^m} \int_{-u}^u \dots \int_{-u}^u \prod_{j=1, j \neq i}^m \mathbb{I}[x_i > x_j] dx_1 \dots dx_m \quad (23)$$

$$= \frac{1}{(2u)^m} \int_{-u}^u \left(\prod_{j=1, j \neq i}^m \int_{-u}^{x_i} \mathbb{I}[x_i > x_j] dx_j \right) dx_i \quad (24)$$

$$= \frac{1}{(2u)^m} \int_{-u}^u \left(\prod_{j=1, j \neq i}^m \int_{-u}^{x_i} dx_j \right) dx_i \quad (25)$$

$$= \frac{1}{(2u)^m} \int_{-u}^u \left(\int_{-u}^{x_i} dy \right)^{m-1} dx_i \quad (26)$$

$$= \frac{1}{(2u)^m} \int_{-u}^u (x_i + u)^{m-1} dx_i \quad (27)$$

$$= \frac{1}{(2u)^m} \cdot \frac{(2u)^m}{m} \quad (28)$$

$$= \frac{1}{m} \quad (29)$$

□

C. Proof of Even Partitioning: Case $K > 1$

For $\Gamma(\theta)$ to evenly partition $\text{unif}(\theta)$, $\theta \in \mathbb{R}^{mK}$, the following must be true for all $\{z_i\}_{i=1}^{m^K} \in \mathcal{Z}^K$.

$$\int_{\mathbb{R}^{mK}} \text{unif}(\theta) \mathbb{I}[z_i = \Gamma(\theta)] d\theta = \frac{1}{m^K} \quad (30)$$

We use the results from Appendices VIII-A and VIII-B to show that the left hand side of the above equation simplifies to $\frac{1}{m^K}$, proving that our relaxation evenly partitions $p_0(\cdot)$. Below, we use the following notation: $\mathbf{u} = [u \dots u] \in \mathbb{R}^m$, $(z_i)_k$ is the k th m -dimensional one-hot vector within $z_i \in \mathcal{Z}^K$, and $\theta_k = \theta_{(k-1)m+1:km} \in \mathbb{R}^m$.

$$\text{LHS} = \int_{\mathbb{R}^{mK}} \text{unif}(\theta) \prod_{k=1}^K \mathbb{I}[(z_i)_k = \max(\theta_k)] d\theta \quad (31)$$

$$= \frac{1}{(2u)^{mK}} \prod_{k=1}^K \int_{-\mathbf{u}}^{\mathbf{u}} \mathbb{I}[(z_i)_k = \max(\theta_k)] d\theta_k \quad (32)$$

$$= \frac{1}{(2u)^{mK}} \prod_{k=1}^K \frac{(2u)^m}{m} \quad (33)$$

$$= \frac{1}{(2u)^{mK}} \cdot \frac{(2u)^{mK}}{m^K} \quad (34)$$

$$= \frac{1}{m^K} \quad (35)$$

□

IX. STAMP PROBLEM FORMULATION AND METHODOLOGY

A. STAMP Pseudocode

Algorithm 1: Stein TAMP (STAMP)

```

1 let: step size =  $\epsilon$ , phase = SVGD
2 initialize:  $n$  particles (candidate task and motion
   plans)  $\{\theta_i\}_{i=1}^n$  randomly, where
    $\theta_i = [a_{1:K}, u_{0:KT-1}]_i$ 
3 while not converged do
   ▷ simulate plans given by each particle in parallel
4    $[x_{1:KT}]_i = f_{\text{sim}}(x_0, \theta_i)$ 
   ▷ compute posterior for all particles in parallel
5    $\rho(\theta_i | O=1) \propto \exp\{-C(\theta_i, [x_{0:KT}]_i)\} \rho(\theta_i)$ 
   ▷ compute update for all particles in parallel
6   if phase = SVGD then
7      $\Delta\theta_i = \frac{1}{w} \sum_{j=1}^n w_j [\nabla_{\theta_j} \log \rho(\theta_j | O=1) k_{ji} + \nabla_{\theta_j} k_{ji}]$ 
     if inference converged then
8        $\text{phase} = \text{SGD}$ 
9   else if phase = SGD then
10     $\Delta\theta_i = \nabla_{\theta_i} \log \rho(\theta_i | O=1)$ 
11     $\theta_i \leftarrow \theta_i + \epsilon \Delta\theta_i$  in parallel

```

B. Use of Dynamic Motion Primitives for Problem Reduction

Dynamic Motion Primitives (DMP) [57] model and generate complex movements by combining a stable dynamical system with transformation functions learned from demonstrations. A movement is modelled with the following system of differential equations:

$$\begin{aligned} \tau \dot{v} &= K(g - x) - Dv - K(g - x_0)s + Kf(s) \\ \tau \dot{x} &= v & f(s) &= \frac{\sum_i w_i \psi_i(s)s}{\sum_i \psi_i(s)} \\ \tau \dot{s} &= -\alpha s \end{aligned} \quad (36)$$

where x and v are positions and velocities; x_0 and g are the start and goal positions; τ is a temporal scaling factor; K and D are the spring and damping constant; s is a phase variable that defines a “canonical system” in equation (36); and $\psi_i(s)$ are typically Gaussian basis functions with different centers and widths. Lastly, $f(s(t))$ is a non-linear function which can be learned to generate arbitrary trajectories from demonstrations. Time-discretized trajectories $x(t), v(t)$ are generated by integrating the system of differential equations in (36). Thus, learning a DMP from demonstrations can be formulated as a linear regression problem given recorded $x(t), v(t)$, and $\dot{v}(t)$.

At runtime, DMPs can be adapted by specifying task-specific parameters x_0 , g , integrating $s(t)$, and computing $f(s)$, which drives the desired behaviour. Our work uses DMPs to generate motion primitives at varying speeds, initial positions, and goals from a small set of demonstrations. DMPs can also be extended to incorporate potential fields [58], [59], [60] to avoid collisions, a key requirement for many motion planning tasks.

X. BILLIARDS PROBLEM SETUP

A. Graphical Overview

A graphical depiction of the billiards problem environment is shown in Figure 8. We recreate this environment in the Warp simulator.

B. Task Variables as Functions of Velocity

We use STAMP to optimize the initial cue ball velocity u_0 and the task plan $z = [z_1, z_2, z_3, z_4] \in \{0, 1\}^4$ where $\forall i \in \{1, 2, 3, 4\}$, $z_i = 1$ if the cue ball bounces off of wall i and $z_i = 0$ otherwise. The walls are labelled 1-4 in Figure 8. In practice, we show that we can relax $z \in \{0, 1\}^4$ into $a = [a_1, a_2, a_3, a_4] \in [0, 1]^4$ and express a as a function of u_0 (see Appendix X-B). This allows us to simply define our SVGD particles as $\theta = [u_0]^\top$, and optimize the task variable implicitly, as a is a function of u_0 and optimizing u_0 will implicitly optimize a . To encourage diversity in the task plans, we employ a along with u_0 within the kernel. We refer the reader to Appendix X-C for details on how the kernel is defined for this problem.

Now we show that the task variable $z_{1:4}$ can be formulated as a soft function of the initial cue ball velocity $u_0 = (v_x, v_y)$. To do so, we first simulate the cue ball's trajectory in a differentiable physics simulator, given the initial cue ball velocity $u_0 = [v_x, v_y]$. We then use the rolled-out trajectory of the cue ball $x_{1:T}^{\text{cue}}$ to define a notion of distance at time t between the cue ball and wall i as follows.

$$d_t^{\text{wall-cue}} = -\alpha \text{SignedDistance}(x_t^{\text{cue}}, \text{wall}_i) + \beta \quad (37)$$

In the above, $\alpha > 0, \beta \in \mathbb{R}$ are hyperparameters that can be tuned to scale and shift the resulting value.

Then, we use $d_t^{\text{wall-cue}}$ to formulate the task variable $z_{1:4}$ as a soft function of u_0 as follows.

$$z_i = \frac{1}{1 + \exp\{-d_{\text{weighted}}\}}, \quad (38)$$

$$d_{\text{weighted}} = \sum_{t=1}^{t_c} \sigma_t d_t^{\text{wall-cue}}, \quad (39)$$

$$\sigma_t = \frac{\exp\{d_t^{\text{wall-cue}}\}}{\sum_{k=1}^{t_c} \exp\{d_k^{\text{wall-cue}}\}} \quad (40)$$

Although z_i is not directly related to u_0 , we note that both quantities are related implicitly since $d_t^{\text{wall-cue}}$ is a function of x_t^{cue} , which result from simulating the cue ball forward using u_0 as the initial ball velocity.

We note that the above formulation of z_i gives us the binary behavior we want for the task variable, but in a relaxed way. That is, z_i will either take on a value close to 1 or close to

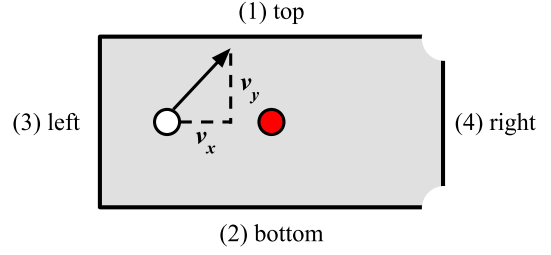


Fig. 8. Graphical depiction of the billiards problem environment. The goal is to shoot the target ball (red) into one of the pockets on the right by finding an initial velocity for the cue ball (white). The task plan is given by the wall(s) the cue ball should hit before hitting the target ball.

0. Intuitively, the sigmoid function will assign a value close to 1 to z_i if the negative signed distance between the wall i and the cue ball is large at some point in the cue ball's trajectory up until t_c , which is the time of contact with the target ball. This can only occur if the cue ball hits wall i at some point in its trajectory before time t_c . Conversely, if the cue ball remains far from wall i at every time step up to t_c , z_i will correctly evaluate to a value close to 0. Note that α and β can be tuned to get the behavior we want for z_i .

Critically, we note that the above formulation is differentiable with respect to u_0 . By relaxing z_i using a sigmoid function over d_{weighted} and using a differentiable physics simulator to roll out the cue ball's trajectory, we effectively construct z_i as soft and differentiable functions of u_0 . The differentiability of z_i with respect to u_0 is important; because of the way we formulate the kernel (see Appendix X-C), the repulsive force $\nabla_{\theta} k(\theta, \theta')$ in the SVGD update requires gradients of z_i with respect to u_0 via the chain rule.

C. Kernel Definition

In SVGD, the kernel is used to compute a kernel-weighted sum of the gradient of the log posterior and to compute repulsive force. The kernel must be positive-definite.

We build upon the Radial Basis Function (RBF) kernel, a popular choice in the SVGD literature, to design a positive definite kernel for $\theta = [v_x, v_y]^\top$. Whereas RBF kernels operate over θ , we operate the RBF kernel over $[\theta, z_{1:4}(\theta)]^\top$, and tune separate kernel bandwidths for $v_{x,y}$ and $z_{1:4}(v_{x,y})$, which we denote as $s_{v_{x,y}}$ and s_z , respectively. This is to account for differences in their range. We use the median heuristic [61] to tune the kernel bandwidths.

$$k(\theta, \theta') = \exp \left\{ -\frac{\|\theta - \theta'\|_2^2}{s_{v_{x,y}}^2} - \frac{\|z_{1:4}(\theta) - z_{1:4}(\theta')\|_2^2}{s_z^2} \right\} \quad (41)$$

D. Loss Definitions

We define the target and aim loss for the billiards problem below. Given the final state at time T of the target ball x_T^{target} , the position of the top pocket g_{top} , the position of the bottom pocket g_{bottom} , and the radius R of the balls, the target loss is defined as the following.

$$L_{\text{target}} = \min(\|x_T^{\text{target}} - g_{\text{top}}\|_2^2, \|x_T^{\text{target}} - g_{\text{bottom}}\|_2^2) \quad (42)$$

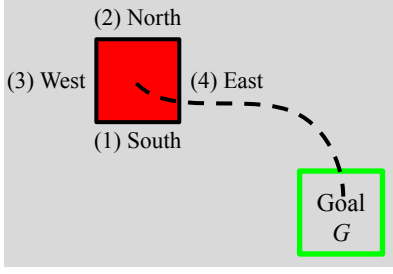


Fig. 9. Graphical depiction of the block-pushing problem environment. The goal is to push the red block into the green goal region by repeatedly applying pushes to either north, south, west, or east of the red block, where these directions are defined relative to the *cube's frame of reference*. The task plan is given by the side(s) to push from.

To define the aim loss, we first introduce the time-stamped aim loss $L_{\text{aim}}^{(t)}$ which is equal to the distance between the closest points on the surface of the target ball and the surface of the cue ball at time t :

$$L_{\text{aim}}^{(t)} = \max(0, |x_t^{\text{target}} - x_t^{\text{cue}}| - 2R) \quad (43)$$

The aim loss L_{aim} is the softmax-weighted sum of the time-stamped aim loss throughout the cue ball's time-discretized trajectory up until time t_c , which is the time of first contact with the target ball.

$$L_{\text{aim}} = \sum_{t=1}^{t_c} \sigma_t L_{\text{aim}}^{(t)}, \quad \sigma_k = \frac{\exp\{-L_{\text{aim}}^{(k)}\}}{\sum_{t=1}^{t_c} \exp\{-L_{\text{aim}}^{(t)}\}} \quad (44)$$

XI. BLOCK-PUSHING PROBLEM SETUP

A. Graphical Overview

Figure 9 shows a graphical overview of the block-pushing problem environment, which we recreate in the Warp simulator. There are a total of four sides to push against: North, South, East, and West. Each of these constitute one symbolic action (e.g., “push the North side”); hence, the action space is $|\mathcal{Z}| = 4$. We represent each action numerically via one-hot encodings of size 4, by assigning each side to numbers 1-4 as shown in the figure.

B. Formulation of the Posterior Distribution

Recall that the total cost function is defined:

$$C(\theta) = \beta_{\text{target}} L_{\text{target}}(x_{KT}) + \beta_{\text{traj}} L_{\text{traj}}(g_{1:K}^{x,y}) \quad (45)$$

The target loss L_{target} measures the proximity of the cube to the goal at the end of simulation, i.e. at timestep KT , and is defined as the following.

$$L_{\text{target}} = \max(0, |x_T^{\text{block}} - g_x| - t)^2 + \max(0, |x_T^{\text{block}} - g_y|)^2 \quad (46)$$

The target loss forms our likelihood distribution $p(O = 1|\theta) \propto \exp(-\beta_{\text{target}} L_{\text{target}})$.

The trajectory loss is a function of $g_k^{x,y} \forall k = 1, \dots, K$ and penalizes the pursuit of indirect paths to the goal. We define

it as:

$$L_{\text{traj}}(g_{1:K}^{x,y}) = \sum_{k=1}^K \left(D_{\text{MH}}(g_{k-1}^{x,y}, g_k^{x,y}) \right. \quad (47)$$

$$\left. + D_{\text{MH}}(g_k^{x,y}, g_K^{x,y}) \right) \quad (48)$$

$$- D_{\text{MH}}(g_{k-1}^{x,y}, g_K^{x,y}) \quad (49)$$

where $D_{\text{MH}}(\cdot)$ is the Manhattan distance function and we use the convention $g_{x,y}^{(0)} = x_0^{\text{cube}}$ to denote the cube's starting state. As L_{traj} is a function only of $g_k^{x,y}$, it forms the prior $p(g_{1:K}^{x,y})$. In particular, we notice that

$$p(g_{1:K}^{x,y}) = \prod_{k=1}^K p(g_k^{x,y} | g_{k-1}^{x,y}) \quad (50)$$

$$p(g_{x,y}^k | g_{k-1}^{x,y}) \propto \exp\left(-D_{\text{MH}}(g_{k-1}^{x,y}, g_k^{x,y}) \right. \quad (51)$$

$$\left. - D_{\text{MH}}(g_k^{x,y}, g_K^{x,y}) \right) \quad (52)$$

$$+ D_{\text{MH}}(g_{k-1}^{x,y}, g_K^{x,y}) \quad (53)$$

The posterior distribution that we run inference over is the product of the likelihood and prior over the intermediate goals.

$$p(\theta | O = 1) \propto p(O = 1|\theta)p(\theta)$$

$$\propto \exp\{-\beta_{\text{target}} L_{\text{target}}(x_{KT})\} \cdot \exp\{-\beta_{\text{traj}} L_{\text{traj}}(g_{1:K}^{x,y})\} \quad (54)$$

C. Kernel Definition

In SVGD, the kernel is used to compute a kernel-weighted sum of the gradient of the log posterior and to compute repulsive force. The kernel must be positive-definite.

We employ the additive property of kernels to construct our positive-definite kernel. The kernel is a weighted sum of the RBF kernel over $\{g_k^{x,y}\}_{k=1}^K$, the RBF kernel over $\{\text{softmax}(a_k)\}_{k=1}^K$, and the von Mises kernel over $\{g_k^\phi\}_{k=1}^K$. The von Mises kernel is a positive definite kernel designed to handle angle wrap-around.

$$K(\theta, \theta') = \sum_{k=1}^K \left[\alpha_{g^{x,y}} K_{\text{RBF}}(g_k^{x,y}, g_k^{x,y'}) \right. \\ \left. + \alpha_z K_{\text{RBF}}(\text{softmax}(a_k), \text{softmax}(a'_k)) \right. \\ \left. + \alpha_{g^\phi} K_{\text{VM}}(g_k^\phi, g_k^{\phi'}) \right] \quad (55)$$

D. Further Results

Figure 12 shows sample solutions obtained from running STAMP on the block pushing problem.

XII. PICK-AND-PLACE PROBLEM SETUP

A. Graphical Overview

The goal of the pick-and-place problem is to place block 1 into either of the two targets, \mathcal{A}, \mathcal{B} , without placing it on top of blocks 2 or 3 which occlude the targets. Correct solutions to this problem involve displacing either block 2 or 3 from the targets and placing block 1 into the empty target. Figure

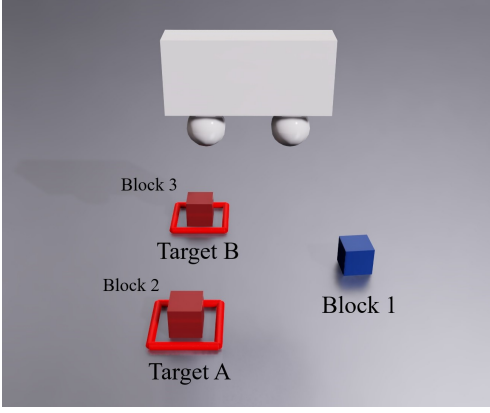


Fig. 10. Graphical depiction of the pick-and-place problem environment.

10 shows a graphical depiction of the problem environment, created and rendered in the Warp simulator. The gripper (or robot end effector) is used to manipulate the blocks.

B. Precondition and Postcondition Loss Definitions

Symbolic actions for the pick-place environment include $Z = \{\text{pick}(\text{cube}), \text{place}(\text{cube})\} \forall \text{cube} \in \mathcal{C}$ (where $\mathcal{C} = \{\text{cube1}, \text{cube2}, \text{cube3}\}$).

Preconditions for $\text{pick}(\text{cube})$ are $\text{pre}(\text{pick}(\text{cube})) = \{\text{eeFree}, \text{canGrasp}(\text{cube}, g)\}$ – that is, the end effector is free and the at goal g the cube is graspable. Postconditions for $\text{pick}(\text{cube})$ are $\text{post}(\text{pick}(\text{cube})) = \{\text{eeHolding}(\text{cube})\}$ – that is, the end effector is holding the cube. Meanwhile, $\text{pre}(\text{place}(\text{cube})) = \{\text{eeHolding}(\text{cube}), \text{canPlace}(\text{cube}, g)\}$; that is, the end effector is holding the cube and the cube can be placed at goal g . Finally, $\text{post}(\text{place}(\text{cube})) = \{\text{eeFree}\}$.

In general, precondition losses are defined w.r.t. the initial states x_{t_0} and pre-emptively sampled goal state g (from the particle), while postcondition losses are defined w.r.t. the final states x_{t_T} . Pre/postcondition losses can be defined differentially, in many cases, through the use of squared distance functions; see the following subsections for details.

1) *Loss for Condition eeFree* $\rightarrow L_{\text{eeFree}}$: eeFree is the condition in which the robot end effector is not holding an object. The associated loss function L_{eeFree} is minimized (evaluates to ≈ 0) if $\text{eeFree}=\text{True}$.

We first define two distance metrics, $d_{\text{ee-c}}$ and d_{grippers} , which are shifted forms of the squared distance function. $d_{\text{ee-c}}^{(t)}$ measures the distance between the end effector and cube c at time t , while $d_{\text{grippers}}^{(t)}$ measures the distance between the grippers at time t . These can be expressed as:

$$d_{\text{ee-c}}^{(t)} = \text{dist}(x_t^{\text{ee}}, x_t^c) \quad (56)$$

$$d_{\text{grippers}}^{(t)} = \text{dist}(x_t^{\text{left gripper}}, x_t^{\text{right gripper}}) \quad (57)$$

where $\text{dist}(\cdot)$ represents the distance function. When the end effector is holding onto cube c , the grippers are closed and the distance between the end effector and the cube is minimized; thus, $d_{\text{ee-c}}, d_{\text{grippers}} \approx 0$. Meanwhile, when $\text{eeFree}=\text{True}$, $d_{\text{ee-c}}, d_{\text{grippers}} \gg 0$.

We define the eeFree loss L_{eeFree} as:

$$L_{\text{eeFree}}(x_t) = \max_c (L_{\text{eeFree},c}(x_t)), \quad (58)$$

where

$$L_{\text{eeFree},c}(x_t) = -\log \left(1 - \exp \left(-d_{\text{ee-c}}^{(t)} - d_{\text{grippers}}^{(t)} \right) \right). \quad (59)$$

$L_{\text{eeFree},c} > 0$ grows large as both $d_{\text{ee-c}}, d_{\text{grippers}} \rightarrow 0$ (i.e., as the probability that the end effector is holding c increases). Since $L_{\text{eeFree}}(x_t) > 0$ equals $L_{\text{eeFree},c} > 0$ for the cube c with the highest probability of being ‘held’ by the gripper, if $L_{\text{eeFree}}(x_t) \rightarrow 0$, there is a high likelihood that $\text{eeFree}=\text{True}$.

2) *Loss for Condition eeHolding(c)* $\rightarrow L_{\text{eeHolding}(c)}$: The loss function for $\text{eeHolding}(c)$ is simply the sum of the distance functions between the end effector and cube c , as well as between the grippers:

$$L_{\text{eeHolding}(c)}(x_t) = d_{\text{ee-c}}^{(t)} + d_{\text{grippers}}^{(t)} \quad (60)$$

$L_{\text{eeHolding}(c)} \geq 0$ is optimal when $d_{\text{ee-c}}, d_{\text{grippers}} \approx 0$, which is true when the end effector is holding cube c .

3) *Loss for Condition canGrasp(c,g)* $\rightarrow L_{\text{canGrasp}(c,g)}$: $\text{canGrasp}(c,g) = \text{True}$ when the end effector can grasp cube c , and it is False otherwise. There are two conditions that must be satisfied for $\text{canGrasp}(c,g) = \text{True}$: first, cube c must be graspable (e.g., no other cubes are stacked on top); second, the cube is graspable at the pre-emptively sampled goal pose g .

$L_{\text{canGrasp}(c,g)}$ is the sum of losses that express these two conditions:

$$L_{\text{canGrasp}(c,g)}(x_t, g) = L_{\text{cubeFree}(c,g)}(x_t) + d_{c-g}^{(t)}(x_t, g), \quad (61)$$

where $L_{\text{cubeFree}(c)} \geq 0$ is optimal ($= 0$) when no cubes are stacked above c and is otherwise equal to the squared vertical distance, $\text{distVertical}(\cdot)$, between c and the cube stacked directly above it.

$$L_{\text{cubeFree}(c)} = \begin{cases} 0 & \text{if } \text{height}(x_t^c) \geq \text{height}(x_t^j) \forall j \in \mathcal{C}, j \neq c, \\ \min_{j \in \mathcal{C}, j \neq c} (\text{distVertical}(x_t^c, x_t^j)) & \text{otherwise} \end{cases} \quad (62)$$

Meanwhile, $d_{c-g}^{(t)}$ measures the squared distance between cube c and the sampled goal pose g .

$$d_{c-g}^{(t)} = \text{dist}(g, x_t^c) \quad (63)$$

4) *Loss for Condition canPlace(c,g)* $\rightarrow L_{\text{canPlace}(c,g)}$: $\text{canPlace}(c,g) = \text{True}$ when two conditions are satisfied: first, the pre-emptively sampled goal pose, g , where the cube c will be placed, must be close to the ground; second, g should not coincide with where other cubes $j \in \mathcal{C}$ are located. We express $L_{\text{canPlace}(c,g)}$ as the following sum:

$$L_{\text{canPlace}(c,g)} = \text{dist}(g, \text{ground}) + \sum_{j \in \mathcal{C}, j \neq c} \exp(-\text{dist}(x_t^j, g)). \quad (64)$$

The first term in the above is minimal when g is close to the ground, while the second term is minimal when all cubes

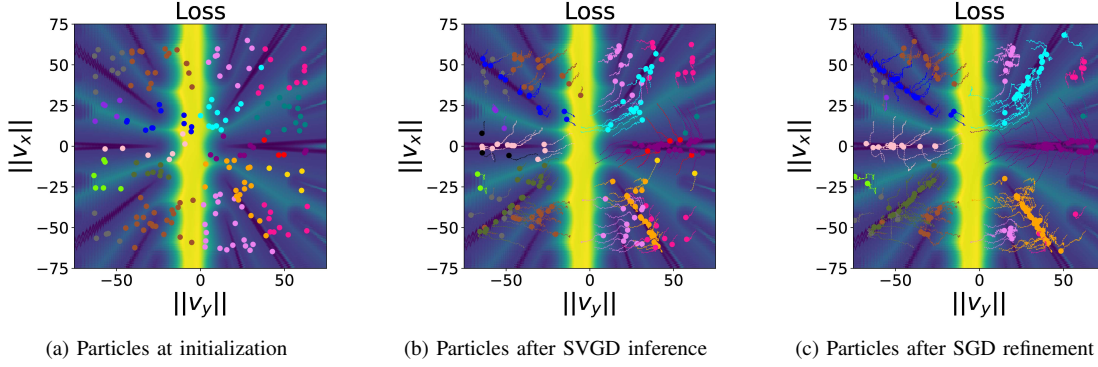


Fig. 11. From left to right: evolution of the distribution of plan parameters θ . On the left, θ are initialized uniformly, while in the middle, they converge to the full likelihood distribution post-SVGD. On the right, the particles collapse to the optima post-SGD. The particles' colors indicate their mode (wall hits).

$j \in \mathcal{C}$ are far from g .

C. Definition of ω_c

We define ω_c as:

$$\omega_c(x_t) = -\log \left(1 - \exp \left(d_{ee-c}^{(t)} - d_{grippers}^{(t)} \right) \right), \quad (65)$$

where $d_{ee-c}^{(t)}$ and $d_{grippers}^{(t)}$ are as defined in section XII-B.

D. Target Loss Definition

$$L_{\text{target},c}(x_{t_T}) = \begin{cases} \text{dist}(x_{t_T}^c, \mathcal{R}) & \text{if } c = \{\text{cube1}, \text{cube2}\}, \\ \mathbb{1}\{\zeta_{\mathcal{A}} \geq \zeta_{\mathcal{B}}\} \cdot \text{dist}(x_{t_T}^{\text{cube1}}, \mathcal{A}) + \\ \mathbb{1}\{\zeta_{\mathcal{A}} < \zeta_{\mathcal{B}}\} \cdot \text{dist}(x_{t_T}^{\text{cube1}}, \mathcal{B}) & \text{otherwise,} \end{cases} \quad (66)$$

where $\mathcal{R} = \neg(\mathcal{A} \wedge \mathcal{B})$, x_t^c is cube c 's position at time t , $\text{dist}(\cdot)$ is a differentiable distance function (e.g. squared distance), and $\zeta_{\mathcal{A}} = \text{dist}(\text{cube2}, \mathcal{A})$, $\zeta_{\mathcal{B}} = \text{dist}(\text{cube3}, \mathcal{B})$ differentiably mimic indicator functions which output a large number when \mathcal{A}, \mathcal{B} are free and 0 if they are occluded by cube1, cube2, respectively.

E. Kernel Definition

As the pick-and-place particle definition is nearly identical to that of the block pushing problem, the kernel is defined similarly. The kernel for the block pushing problem environment is defined in Section XI-C.

F. Exploding Gradient Issues

A potential limitation of employing differentiable simulators is that gradients can explode as the time horizon of the simulation increases. This can be a problem when trying to run STAMP on long-horizon sequential manipulation problems, such as pick-and-place.

Here, we propose a modification to STAMP that mitigates gradient explosion due to long horizon simulation. The key insight we leverage is that the cost function, as defined in equation (16), is expressed entirely as the sum of individual

loss terms which only depend on trajectories within each of the K action sequences; i.e., it is of the form:

$$C(\theta) = \sum_{k=1}^K C_k(a_k, g_k, x_{(k-1)T+1:kT}) \quad (67)$$

As the loss functions within the sums only depend on short trajectories (e.g., $x_{(k-1)T+1:kT}$ as opposed to $x_{1:KT}$) and the task variable a_k , we can split the optimization into smaller chunks by defining the posterior using the 'inner' cost C_k , which prevents the need for taking gradients over the entire trajectory $x_{1:KT}$ and mitigates the danger of gradient explosion during optimization.

XIII. ADDITIONAL RESULTS

A. Block Pushing Results

Figure 12 shows samples of solutions obtained from running STAMP on the block pushing experiment.

B. SVGD-SGD Plan Refinement

Figure 11 shows how the particles move through the loss landscape of the billiards problem. Figure 5 shows how the loss evolves over various iterations of STAMP for the billiards and block-pushing problems.

XIV. IMPLEMENTATION OF BASELINES

For both baselines, the task plan is the walls to hit for the billiards problem and the sequence of sides to push from for the block pushing problem.

A. PDDLStream

PDDLStream combines search-based classical planners with *streams*, which construct optimistic objects for the task planner to form an optimistic plan and then conditionally sample continuous values to determine whether these optimistic objects can be satisfied [4]. Since it is possible to create an infinite amount of streams and thus optimistic objects, the number of stream evaluations required to satisfy a plan is limited and incremented iteratively. As a result, PDDLStream will always return the first-found plan with the smallest possible sequence of actions in our evaluation problems, resulting in no diversity.

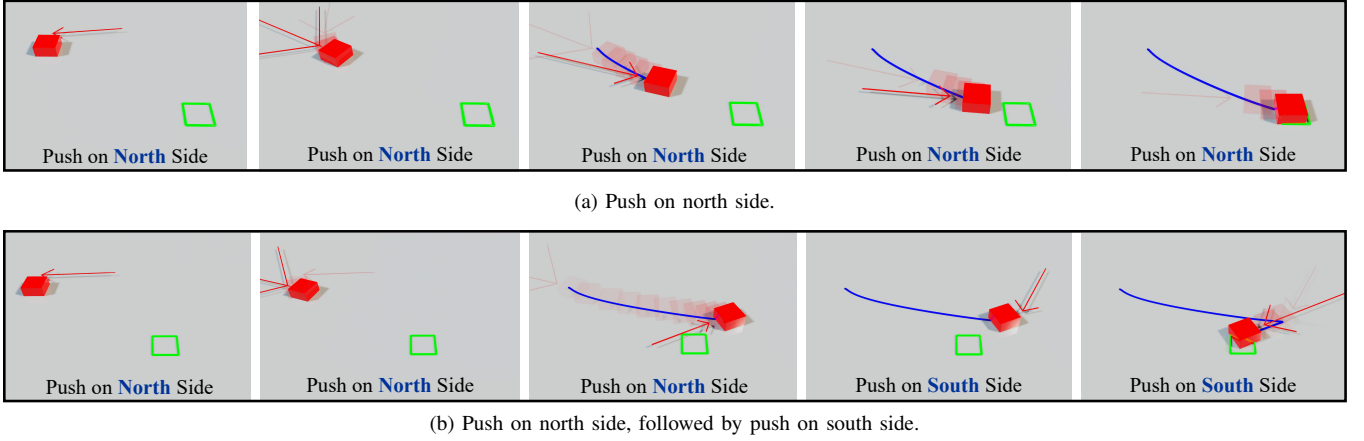


Fig. 12. Sample solutions obtained from running STAMP on the block pushing problem. The red arrow is proportional to the magnitude and direction of the pushing force, the blue line shows the block’s trajectory, and the green box shows the goal region. Note, the notions of ‘north’, ‘south’, ‘east’ and ‘west’ are relative to the cube’s frame of reference (see Figure 9).

To generate different solutions, we force PDDLStream to select different task plans based on some preliminary work in <https://github.com/caelan/pddlstream/tree/diverse>. For the billiards problem, we can reduce the task planning problem by enumerating all possible wall hits and denoting each sequence as a single task, since the motion planning stream is only needed once for any sequence of wall hits. Then, we select a task by uniform sampling and try to satisfy it by sampling initial velocities that match the desired wall hits using SGD and Warp. For the block-pushing problem, we use a top-k or diverse PDDL planner to generate multiple optimistic plans of varying complexity. We then construct the problem environment with the same Warp environment as STAMP and use the pretrained DMPs for the motion planning streams. Note that the distribution of solutions is highly dependent on the time allocated for sampling streams. Of the feasible candidate plans, PDDLStream randomly selects a solution.

B. Logic-Geometric Programming

Diverse LGP [6] uses a two-stage optimization approach by first formulating the problem on a high, task-based level (as an SAS⁺ [62] task). Subsequently, a geometric (motion planning) problem is solved conditioned on the logical plan. That is, the performed motion is required to fulfill the logical plan. A logical plan is called *geometrically infeasible* if there is no motion plan fulfilling it. Diverse LGP speeds up exploration by eagerly forbidding geometrically infeasible plan prefixes (for instance, if moving through a wall is geometrically infeasible, no sequence starting with moving through a wall has to be tested for geometric feasibility).

We use the first iteration of LAMA [63] (implemented as part of the Fast Downward framework [64]) as suggested in [6] and use SGD for motion planning. To enforce diversity in the logical planner, we iteratively generate 25 logical plans by blocking ones we already found. As Diverse LGP finds exactly one solution to the TAMP problem per run, we invoke it as many times as STAMP found solutions to get the same sample size.

For both billiards and block-pushing, we use the SGD component described in Section IV-C. For billiards, we additionally add a loss term ensuring that the required walls are hit. For pusher, it suffices to fix z_1, \dots, z_K in θ . That is, excluding them from the SGD update.